The "α-invariant": An Energy-Based Nonlinear Minimal Damping Model for Robotic Joints With Friction

Dr. Bart Milne
Department of Mechanical Engineering
University of Canterbury
Christchurch 8140, New Zealand
Email: milne.bje@gmail.com

Dr. Chris Hann
Department of Electrical Engineering
University of Canterbury
Christchurch 8140, New Zealand
Email: chris.hann@canterbury.ac.nz

Prof. XiaoQi Chen[*]
Department of Mechanical Engineering
University of Canterbury
Christchurch 8140, New Zealand
Email: xiaoqi.chen@canterbury.ac.nz

System identification of the sinusoidal steady state response of the Phantom Omni using a local linear model revealed that friction has a non-negligible effect on the accuracy of a global linear model, particularly at low frequencies. Some of the obvious errors observed with the global linear model at low frequencies were (i) the response amplitude was lower; (ii) local linear model coefficients became physically impossible (e.g. negative) at low frequencies; and (iii) low frequency inputs resulted in a greater non-linearity in the response compared to higher frequency inputs.

Whilst standard friction models such as Coulomb friction could be used to model the nonlinearity, there is a desire to create a friction model that is not only accurate for sinusoidal steady state responses, but can be generalised to any input response. One measure that is universally present in dynamical systems is energy, and in this paper the relationship between a generalised measure of energy and damping for modelling the effect of friction is developed.

This paper introduces the 'α-invariant' as a means of generalising the friction behaviour observed with sinusoidal steady state responses to other waveforms. For periodic waveforms, the α-invariant is shown to be equivalent to the energy dissipated in each cycle, which demonstrates the physical significance of this quantity. The α-invariant nonlinear model formulation significantly outperforms the linear model for both sinusoidal steady state and step responses, demonstrating that this method accurately represents the physical mechanisms in the Phantom Omni. Overall the α-invariant provides an efficient way of capturing non-linear dynamics with a small number of parameters and experiments.

1 Introduction

Minimal modelling seeks to identify the major dynamics of a system in a form that is easily understood, implemented, and identifiable. System identification using minimal modelling uses governing equations based on physical parameters, and is similar to other papers on the subject that use physically derived models [1–6]. While a minimal model may not capture all dynamics, an elementary minimal model is important for understanding how the identified parameters are affected by changes in the machine over time due to e.g. repairs or changes in mass distribution during operation. The underlying concepts behind minimal modelling are transferable across a wide range of systems, such as diabetes diagnosis and detection [7], mitral valve modelling [8], rocketry [9] and non-linear modelling in a spring cart [10].

System identification of the Phantom Omni is also useful in its own right because stable haptic feedback control requires understanding of its dynamics [11–14]. The minimal model of the Phantom Omni and controller results in a second order state space differential equation with time varying coefficients, similar to the methods outlined in [5,15–17]. The dynamic parameters of the Phantom Omni are identified using sinusoidal steady state analysis, then cross-validated using a step response. While alternative waveforms such as pseudo-random binary sequences (PRBS) can be used to identify the frequency and phase response [18], but the advantage of sinusoidal steady state analysis over PRBS is that non-linearities at a particular frequency are obvious by examining the waveform, and sinusoidal amplitude and phase distortion of the output. Since the Phantom Omni output lacks intermodulation products, any harmonic distortion is assumed solely from actuator non-linearities, changes in joint angles (affecting rotational inertia), and frictional ef-

---

[*]Corresponding author.

fects [6]. While the Phantom Omni's inertia is also a cause of non-linearity, its effect can be eliminated by setting the joint angles constant, so inertia stays constant during a given identification run.

Models of frictional damping include those dependent on velocity [4, 6, 19, 20], and there are many forms that get very complex [3, 5, 21, 22]. Some use autoregressive exogenous (ARX) models [23] or just have high order transfer functions [24]. A limitation of complex friction models is the requirement for extensive experimentation and measurement. Joint friction has also been identified using wavelet methods [25], which have good temporal resolution but the difficulty of assigning the identified coefficients to a physical process makes it is difficult to determine the effects of changes in the machine configuration on the identified model. Naerum [26] is correct in mentioning that unknown parameters can reduce the accuracy of a physical model. Unlike those papers, the objective of this research is to identify the non-linear characteristics of the Phantom Omni as a function of a metric of energy dissipation of the input waveform in each cycle, while utilising a method similar to equating coefficients for fast and accurate system identification. This research does not seek to fully describe the Phantom Omni dynamics in the pitch and yaw, but demonstrate a new concept for capturing complexity in damping and friction behaviour by bootstrapping complex non-linear dynamics from an initial minimal model.

Section 2 discusses in detail the α-invariant non-linear modelling methodology, including the α-invariant derivation, α-invariant for sinusoidal steady state response and numerical simulation and verification. Section 3 presents and discusses the application of the α-invariant model developed in Section 2 for the Phantom Omni. Concluding remarks are given in Section 4.

2 Methodology
2.1 Phantom Omni Experimental Setup
2.1.1 Phantom Omni Definitions

Fig. 1 shows a kinematic diagram of the Phantom Omni with labelled angles and torques. In general, the angles γ_1 and γ_2 were not at the set point during the experiments, due to the combination of gravity loading and the use of proportional controllers. However, the accuracy of γ_1 and γ_2 is not critical, as the inertia model described in Section 2.1.2 uses the true angle values, not the setpoint values.

The physical model of the Phantom Omni is derived using a similar methods to Tahmasebi for the Phantom Premium 1.5 [1]. Equation (1) shows the yaw torque model for the Phantom Omni. The torque $u(t)$ is the torque observed to accelerate the yaw axis from angle measurements, and is the actuator torque with any friction effects taken into account. The yaw axis torque $u(t)$ is defined by:

$$u(t) = \overline{\beta}v(t) - \overline{C}\dot{\theta}(t) \qquad (1)$$

where $v(t)$ is a command voltage applied to the internal motor to generate torque and $\theta(t)$ is the yaw angle. The quantities $\overline{\beta}$ and $\overline{C}$ in (1) are the torque proportionality constant
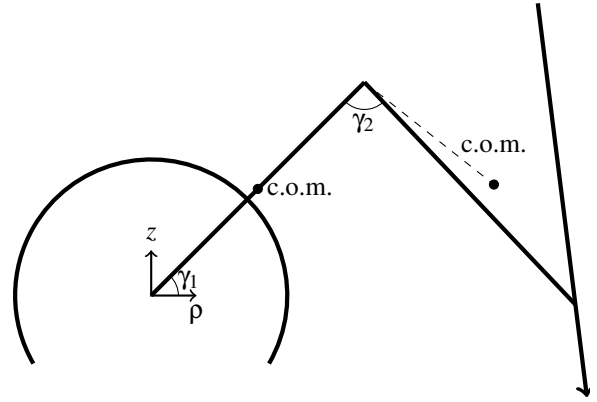

Fig. 1. Simplified diagram of the Phantom Omni showing centre of masses

$(\mathrm{N\,m\,V^{-1}})$ and the viscous damping constant $(\mathrm{N\,m\,s\,rad^{-1}})$ respectively. In the experiments, there was no external load applied to the Phantom Omni, so it is assumed that all of the available torque is used to accelerate the rotating mass of the arm and is defined:

$$u(t) = I\ddot{\theta} \qquad (2)$$

where I is the moment of inertia of the arm about the yaw axis. Substituting (2) into (1) gives the kinematic-dynamic ordinary differential equation (ODE) model (3).

$$I\ddot{\theta} + \overline{C}\dot{\theta} = \overline{\beta}v(t) \qquad (3)$$

The intrinsic yaw axis joint damping and actuator gain ($\overline{C}$ and $\overline{\beta}$ respectively) are defined as properties of the joint itself and thus do not depend on inertia. However, $\overline{C}$ and $\overline{\beta}$ can be affected by the friction in the joint. The intrinsic damping and actuator gain are independent of the joint angle because the yaw axis has no torsional spring and its axis is vertical and not affected by gravity. In the special case of a linear system with a sine wave input at a fixed frequency $\overline{C}$ and $\overline{\beta}$ are constant due to the inertia being constant and α being an invariant for a fixed frequency sine wave. Equation (3) accurately reflects the physical setup but includes the inertia, which depends on the masses present in the arm and their distribution. Dividing through by inertia and using substitutions $C = \frac{\overline{C}}{I}$ and $\tilde{\beta} = \frac{\overline{\beta}}{I}$ yields the simplified model

$$\ddot{\theta} + C\dot{\theta} = \tilde{\beta}v(t) \qquad (4)$$

which is linear for constant inertia. Thus, the inertia is "lumped" into C and $\tilde{\beta}$ in (4) and direct knowledge of the intrinsic physical properties of the arm is *not* required to model its behaviour.

2.1.2 Yaw Axis Inertia Model

A minimal yaw axis inertia model is derived by assuming the arm links are uniform thin rods. The basic inertia model is then used as a basis for deriving the modified inertia model for modelling C and $\tilde{\beta}$ as a function of the joint angles. Fig. 1 shows the approximate centres of masses of the respective arm segments and central shell obtained from measurements of the arm segments from a spare Phantom Omni. The

reference axis for the parallel axis theorem is the z (yaw) axis and the radial distance for the parallel axis theorem is measured along the ρ axis. Equation (5) shows the basic inertia of the arm, where I_{base} is the inertia of the base and m_n and L_n are the respective masses and lengths of Link n.

$$I = I_{\text{base}} + \frac{1}{3}m_1 L_1^2 \cos^2(\gamma_1) + m_2$$
$$\cdot \left(L_1 \cos(\gamma_1) + \frac{1}{2}L_2 \cos(\pi - \gamma_1 - \gamma_2 - \gamma_{\text{offs}})\right)^2 \quad (5)$$
$$+ \frac{1}{12}m_2 L_2^2 \cos^2(\pi - \gamma_1 - \gamma_2 - \gamma_{\text{offs}})$$

Although (5) could be used to generate the inertia model directly from the masses and lengths of the Phantom Omni arm, the system identification uses the minimal inertia model (6), created by lumping the trigonometric coefficients together. The decoupling of the inertia model coefficients from the masses and lengths allows more freedom in the inertia model, in particular it means detailed information about the mass and length of the arm segments is not as important, due to the "float" introduced into the minimal model.

$$I = I_{\text{base}} + I_1 \cos^2(\gamma_1) + I_2 \cos^2(\pi - \gamma_1 - \gamma_2 - \gamma_{\text{offs}}) \quad (6)$$
$$+ I_3 \cos(\gamma_1)\cos(\pi - \gamma_1 - \gamma_2 - \gamma_{\text{offs}})$$

The advantage of having an inertia model is that it makes use of the fact that the Phantom Omni's response in (3) is not dependent on the numerical values of I, $\overline{C}$ and $\tilde{\beta}$ in themselves, but their ratios. The modified inertia model is implemented by fixing the value of $\overline{\beta}$ to 1, so that C and $\tilde{\beta}$ have a fixed relationship to inertia, as shown in (7) and (8). The damping ratio C_0 introduced in (8) has the property $\overline{C}_0 = \frac{\overline{\beta}}{\overline{C}}$.

$$\tilde{\beta} \triangleq \frac{1}{I} \quad (7)$$

$$C \triangleq \frac{1}{\overline{C}_0 I} \quad (8)$$

2.2 System Identification

Although the research was carried out on a Phantom Omni, the target systems of this research can be generalised to ones that control a process value (e.g. position or angle) with an actuator that outputs a force value (e.g. force or torque). The discussion in this section will use the terminology of a position controller with a force actuator. The controller is assumed to be single input-single output (SISO), but cross coupling effects from other controllers can be modelled as disturbances.

2.2.1 PID Controller

The system identification of the Phantom Omni in this paper is performed using a conventional proportional-integral-derivative (PID) controller. The yaw angle error $e(t)$ for a given input $r(t)$ and measured angle $\theta(t)$ is shown in (9), and the PID output $v(t)$ is shown in (10), where k_{p}, k_{i} and k_{d} are the proportional, integral and derivative control coefficients respectively.

$$e(t) = r(t) - \theta(t) \quad (9)$$

$$v(t) = k_{\text{p}}e(t) + k_{\text{i}} \int_0^t e(\tau)\,d\tau + k_{\text{d}}\frac{de}{dt} \quad (10)$$

2.2.2 Actuator

The actuator converts the force command and disturbance force commands into position. The actuator is assumed to have viscous damping but have no spring effect. Equation (11) shows the transfer function from force to position, where C is the viscous damping and $\tilde{\beta}$ is the actuator gain. It is assumed the disturbance term $n(t)$ represents a disturbance that is not linearly related to the output (e.g. a gravitational load when the joint is driven by a sine wave), so that if the disturbance is linearly related to the output it can be identified by its effect on C and $\tilde{\beta}$.

$$\ddot{\theta} + C\dot{\theta} = \tilde{\beta} \cdot (v(t) + n(t)) \quad (11)$$

2.2.3 Closed Loop System Identification

The system identification is based on the closed loop dynamic equation (12), formed by combining (9), (10) and (11).

$$\ddot{\theta} + (C + \tilde{\beta}k_{\text{d}})\dot{\theta} + \tilde{\beta}k_{\text{p}}\theta(t) + \tilde{\beta}k_{\text{i}} \int_0^t \theta(\tau)\,d\tau$$
$$= \tilde{\beta}k_{\text{p}}r(t) + \tilde{\beta}k_{\text{i}} \int_0^t r(\tau)\,d\tau + \tilde{\beta}k_{\text{d}}\frac{dr}{dt} + \tilde{\beta}n(t) \quad (12)$$

Equation (12) is modified by setting $k_{\text{i}} = 0$ and $k_{\text{d}} = 0$ to give the identification equation (13). Eliminating the integral coefficient simplifies the equation, and eliminating k_{d} means that C is identified directly. During identification, the actuator gain is lumped with the proportional gain by setting $\beta = \tilde{\beta}k_{\text{p}}$, as this is the quantity that will be identified.

$$\ddot{\theta} + C\dot{\theta} + \beta\theta = \beta r \quad (13)$$

2.2.4 Local Linear Model

For a given inertia, the parameters C and β in (4)-(13) are initially assumed constant over time. In practice, they may not be constant and could change depending on various non-linearities of the system. To capture this non-linearity, these parameters are first assumed to be a function of frequency. The C and β coefficients are identified using sinusoidal steady state analysis, using (13) and $r(t) = A_{\text{r}}\sin(\omega t)$ as the input, and approximating the steady state output as a sinusoid. The sinusoidal coefficients are identified in Cartesian form (14) using the linear least squares equation (15), where $\mathbf{t}$ is the vector of time values during the steady state response.

$$\theta(t) = A_1 \cos(\omega t) + A_2 \sin(\omega t) \quad (14)$$

$$[\cos(\omega \mathbf{t})\ \sin(\omega \mathbf{t})]\begin{bmatrix} A_1 \\ A_2 \end{bmatrix} = [\theta] \quad (15)$$

The coefficient equations are developed using $\theta(t)$'s polar form (16), where $A_0 = \sqrt{A_1^2 + A_2^2}$ and $\phi = \arctan\left(\frac{A_1}{A_2}\right)$. The polar form is used with the differential equation as it is easier to work with.

$$\theta(t) = A_0 \sin(\omega t + \phi) \tag{16}$$

The basic formula for equating coefficients (17) is created by substituting (16) into (13).

$$-\omega^2 A_0 \sin(\omega t + \phi) + \omega C A_0 \cos(\omega t + \phi) \\ + \beta A_0 \sin(\omega t + \phi) = \beta A_r \sin(\omega t) \tag{17}$$

The simultaneous equations (18) are created using trigonometric expansions on (17), substituting $A_1 = A_0 \sin\phi$, $A_2 = A_0 \cos\phi$ and separating the cosine and sine coefficients.

$$-\omega^2 A_1 + \omega A_2 C + A_1 \beta = 0 \\ -\omega^2 A_2 + \omega A_1 C + (A_2 - A_r)\beta = 0 \tag{18}$$

The calculated C and β are shown in (19) and (20). They are denoted with a "data" suffix as they are used for input to the non-linear damping and resonant frequency models.

$$C_{\text{data}}(\omega) = -\frac{\omega A_r A_1}{A_1^2 + A_2(A_2 - A_r)} \tag{19}$$

$$\beta_{\text{data}}(\omega) = \frac{\omega^2(A_1^2 + A_2^2)}{A_1^2 + A_2(A_2 - A_r)} \tag{20}$$

Friction affects the response at low frequencies by producing an 'excessive' attenuation for the phase shift [27]. At very low frequencies, if $A_r A_2 > A_1^2 + A_2^2$, or $A_r A_0 \cos\phi > A_0^2$, the identified single frequency C_{data} and β_{data} become negative. These frequencies are excluded from the α-invariant model calculations, as the data obtained is not physically possible. The identified $C_{\text{data}}(\omega)$ and $\beta_{\text{data}}(\omega)$ are used as inputs with the α-invariant based nonlinear model.

2.2.5 Global Linear Model

A global linear model is created using (18) on all the single frequency A_1 and A_2 values simultaneously. The linear dynamic model is given in (21). Note this equation has an identical form to (13), but is repeated with linearised parameters for clarity.

$$\ddot{\theta} + C_{\text{linear}}\dot{\theta}(t) + \beta_{\text{linear}}\theta(t) = \beta_{\text{linear}} r(t) \tag{21}$$

The goal is to use (21) to identify β_{linear} and C_{linear}, then use the identified global linear parameters as a basis for modelling the inertia. The linear parameters are found using a linear regression using an all-frequency version of Equation (18):

$$\begin{bmatrix} \omega \circ \mathbf{A}_2 & \mathbf{A}_1 \\ \omega \circ \mathbf{A}_1 & \mathbf{A}_2 - A_r \end{bmatrix} \begin{bmatrix} C_{\text{linear}} \\ \beta_{\text{linear}} \end{bmatrix} = \begin{bmatrix} \mathbf{A}_1 \circ \omega^2 \\ \mathbf{A}_2 \circ \omega^2 \end{bmatrix} \tag{22}$$

where

$$\omega = [\omega_1, \omega_2, \cdots, \omega_n]^T \\ \omega^2 = \omega \circ \omega = [\omega_1^2, \omega_2^2, \cdots, \omega_n^2]^T \\ \mathbf{A}_1 = [A_1(\omega_1), A_1(\omega_2), \cdots, A_1(\omega_n)]^T \\ \mathbf{A}_2 = [A_2(\omega_1), A_2(\omega_2), \cdots, A_2(\omega_n)]^T \tag{23}$$

and the symbol $\circ$ represents the Hadamard (element wise) product of two vectors or matrices. The calculated C_{linear} and $\tilde{\beta}_{\text{linear}}$ at each set of joint angles are used to develop the inertia model, provide initial conditions for the non-linear dynamics model explained in 2.4.1, and develop the model of C and β in terms of the α-invariant as disclosed later in the article. The effects of inertia are modelled by the asymptotic curves in a similar way to (40) and (42):

$$C_{\text{linear}}(I) = \frac{1}{\overline{C}_0 I} \tag{24}$$

$$\beta_{\text{linear}}(I) \triangleq \frac{1}{I} \tag{25}$$

where the inertia I is the modified inertia model (6). The resulting linear approximate model is defined:

$$\ddot{\theta} + C_{\text{linear}}(I)\dot{\theta} = \tilde{\beta}_{\text{linear}}(I)v(t) \\ \tilde{\beta}_{\text{linear}}(I) = \frac{\beta_{\text{linear}}(I)}{k_p} \tag{26}$$

Equation (26) is non-linear with respect to inertia, but if inertia stays constant the yaw response is linear, hence the justification of referring to (26) as "global linear" for comparison with the non-linear model.

2.2.6 Inertia Model

The I_{base}, I_1, I_2, I_3, γ_{offs} and $\overline{C}_0$ coefficients are found using non-linear least squares solver with a test function created by combining (6), (7) and (8). The input consists of γ_1, γ_2, $\tilde{\beta}_{\text{linear}}$ and C_{linear} from the fitted sine wave sweeps. The full regression equations are shown in (27)-(29). The vector forms represent the complete sets of γ_1, γ_2, $\tilde{\beta}_{\text{linear}}$ and C_{linear}. The modified inertia model is considered physically valid if I_{base}, I_1, I_2 and I_3 are non-negative, as this condition corresponds to having positive masses with γ_1 and γ_2 as defined in Fig. 1.

$$\vec{I} = I_{\text{base}} + I_1 \cos^2(\vec{\gamma}_1) + I_2 \cos^2(\pi - \vec{\gamma}_1 - \vec{\gamma}_2 - \gamma_{\text{offs}}) \\ + I_3 \cos(\vec{\gamma}_1)\cos(\pi - \vec{\gamma}_1 - \vec{\gamma}_2 - \gamma_{\text{offs}}) \tag{27}$$

$$\vec{\tilde{\beta}}_{\text{linear}} = \frac{1}{\vec{I}} \tag{28}$$

$$\vec{C}_{\text{linear}} = \frac{1}{\overline{C}_0 \vec{I}} \tag{29}$$

The outcome is a non-linear model of inertia that automatically accounts for different distributions in masses without requiring their measurement.

2.3 α-invariant Nonlinear Model

The concept of the alpha-invariant was developed from the observed steady state response to a range of frequencies. Key observations are summarised as follows:

1. the sinusoidal steady state response amplitude was much lower than a typical linearised model would predict;
2. local linear model coefficients became physically impossible at low frequencies. For example, negative values resulted from the 'excessive' phase shift relative to

amplitude;

3. a global linear model was unable to capture the steady state amplitude and phase accurately across all frequencies; and

4. low frequency or lower 'energy' inputs resulted in a greater non-linearity in the response compared to higher frequency/higher energy inputs.

The α-invariant is intended to represent equal effects for a snap-shot in time of a dynamic non-sinusoidal response. For example if there were two points in time with the same α-invariant, then at these times, the instantaneous energy of the output is the same. For perfectly sinusoidal waveforms, the α-invariant or energy dissipated in each cycle is invariant over time, but is not invariant in a transient response. In other words, the term 'invariant' is defined with respect to a subsystem of the full range of possible responses. To further clarify this concept, an analogous invariant in geometrical analysis is the Euclidean curvature, which is invariant with respect to rotations and translations, but not invariant under scaling transformations.

2.3.1 α-invariant Derivation

As stated previously, non-linearities in the identified single frequency parameters cause C_{data} and β_{data} to vary with amplitude and frequency. The aim of the α-invariant is to describe the damping and actuator gain derived from the sinusoidal steady state response in terms of a parameter that does not explicitly have the amplitude or frequency as an argument. The objective of removing the amplitude and frequency dependence is to be able to generalise the damping behaviour identified from the sine wave to any input waveform. The α-invariant is derived from the properties of a sinusoidal wave and its derivatives. For a sinusoidal wave $v = A\sin(\omega t + \phi)$, the phase portrait $(v, \dot{v})$ is an ellipse. The standard equation for this ellipse in terms of v and $\dot{v}$ is defined:

$$\frac{v^2}{a^2} + \frac{\dot{v}^2}{b^2} = 1 \qquad (30)$$

Differentiating (30) with respect to t and solving for a^2 yields:

$$a^2 = -\frac{v}{\ddot{v}}b^2 \qquad (31)$$

Substituting (31) into (30) gives a formula for b^2 in terms of the intrinsic properties of the curve $(v, \dot{v})$:

$$b^2 = \dot{v}^2 - v\ddot{v} \qquad (32)$$

Equation (32) motivates the definition of the α-invariant:

$$\alpha = \dot{v}^2 - v\ddot{v} \qquad (33)$$

The α-invariant is geometrically equivalent to the square of the vertical distance of the ellipse in (30). Thus, for a sinusoidal response, the α-invariant represents the energy supplied. In other words, for any sinusoidal input $v(t)$, the value of α is an invariant. The advantage of the α-invariant formulation is that it gets rid of direct dependence on the wave shape and the frequency. The α-invariant value is considered

valid if it is a real number. For (33), this condition is met if $v(t)$ has at least $\mathbb{C}^1$ continuity. Non-sinusoidal periodic waveforms will in general have a varying α-invariant during a cycle. However, the α-invariant can be reformulated as an average over an entire cycle to derive an sine wave equivalent approximation. The approximation is shown in (34), and is valid for any $\mathbb{C}^0$ waveform.

$$\alpha \approx \frac{1}{T}\int_{t_0-T}^{t_0} \dot{v}^2 - v\ddot{v}\,dt \qquad (34)$$

Once the α-invariant model is formulated it can be used to create a model for damping and resonant frequency. The α-invariant can then be calculated in real time, for example for use in a state space formulation. If a physical relationship between C and β is known, the physical model can be used. Otherwise, a piecewise linear model can be developed by inspection of the relationship between a given dynamic parameter and α.

2.3.2 α-invariant for Sinusoidal Steady State Reponse

Substituting $y = A_1\cos(\omega t) + A_2\sin(\omega t)$ and $r(t) = A_{\mathrm{r}}\sin(\omega t)$ into (10) with $k_{\mathrm{i}} = k_{\mathrm{d}} = 0$ gives the input voltage (35).

$$v(t) = k_{\mathrm{p}} \cdot (-A_1\cos(\omega t) + (A_{\mathrm{r}} - A_2)\sin(\omega t)) \qquad (35)$$

The input voltage $v(t)$ in (35) is substituted into (33) and simplified to give an analytical expression for the α-invariant defined:

$$\alpha = k_{\mathrm{p}}^2\omega^2(A_1^2 + (A_{\mathrm{r}} - A_2)^2) \qquad (36)$$

Since α is a function of ω and the amplitudes, it can automatically account for frequency changes, which is useful for characterising the values of C and $\tilde{\beta}$ across a range of frequencies. Specifically, the parameters C and $\tilde{\beta}$ in (11) are written as functions of α, which corresponds to the model:

$$\ddot{\theta} + C(\alpha)\dot{\theta} = \tilde{\beta}(\alpha)v(t) \qquad (37)$$

The quantities C and $\tilde{\beta}$ in (37) may also be affected by changes in the state of the device being controlled such as joint states. In this case, the dynamic model (37) can be used for all joint states by determining a relationship between dynamic parameters and the joint states. In that case, C and $\tilde{\beta}$ will depend on the joint states as well as α.

2.3.3 Damping Model

It was observed during the sinusoidal steady state experiments for the global linear model that damping increased with decreasing α. This behaviour is not surprising, since α is related to energy, as at low energy stiction effects dominate, producing a higher damping coefficient. At higher input energies, stiction disappears and the only significant damping is viscous damping. The Phantom Omni's damping as a function of α was found to be representable by a tri-linear piecewise model:

$$C(\alpha, I) = \left[C_0(I) + \frac{C_1(I) - C_0(I)}{\alpha_1 - \alpha_0}(\alpha - \alpha_0) \right] \cdot \Pi_{\alpha_0, \alpha_1}(\alpha)$$
$$+ \left[C_1(I) + \frac{C_2(I) - C_1(I)}{\alpha_2 - \alpha_1}(\alpha - \alpha_1) \right] \cdot \Pi_{\alpha_1, \alpha_2}(\alpha)$$
$$+ \left[C_2(I) + \frac{C_3(I) - C_2(I)}{\alpha_3 - \alpha_2}(\alpha - \alpha_2) \right] \cdot \Pi_{\alpha_2, \alpha_3}(\alpha)$$

(38)

where $\Pi_{\alpha_m, \alpha_n}(\alpha) = H(\alpha - \alpha_m) - H(\alpha - \alpha_n)$ is the Boxcar function and $C_0, \ldots, C_3$ are defined

$$\begin{aligned} C_0(I) &= C(\alpha_0, I) \\ C_1(I) &= C(\alpha_1, I) \\ C_2(I) &= C(\alpha_2, I) \\ C_3(I) &= C(\alpha_3, I) \end{aligned}$$

(39)

and $\alpha_0, \ldots, \alpha_3$ are a monotonically increasing series of break points. The result is a set of four damping values $C_0(I), \ldots, C_3(I)$ uniquely characterise the tri-linear approximation to the non-linear damping curve. The values of $\alpha_0, \ldots, \alpha_3$ in (39) are chosen in a grid search to minimize the least squares error. Fig. 2 shows example $C(\alpha, I)$ curves for three monotonically increasing values of inertia, $I_a < I_b < I_c$.
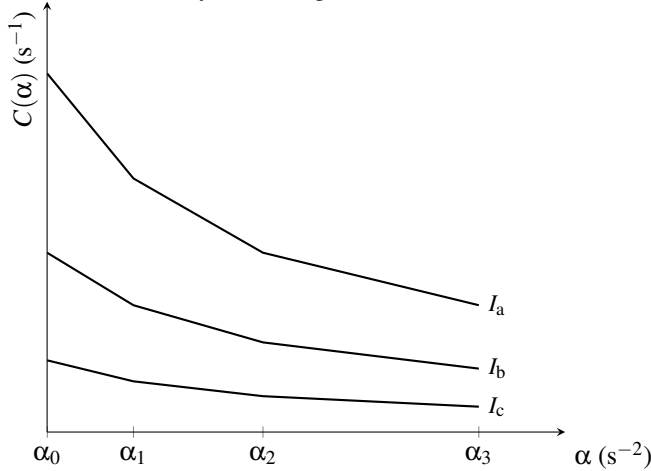

Fig. 2. Illustrative non-linear damping curves as a function of α for various values of inertia

The behaviour of C with respect to I makes physical sense, since a high inertia corresponds to a greater storage of energy and a greater torque for a given angular acceleration. Hence, with higher inertia, viscous friction effects dominate sooner, giving lower damping values for a given value of α. Fig. 3 shows the model used to capture this effect of inertia as an asymptotically decreasing curve, which is used for $C_0(I), \ldots, C_3(I)$ in (39).

Fig. 2 and 3 represent vertical slices of the $C(I, \alpha)$ surface in (37) that correspond to constant I and constant α respectively. The curves are defined by:
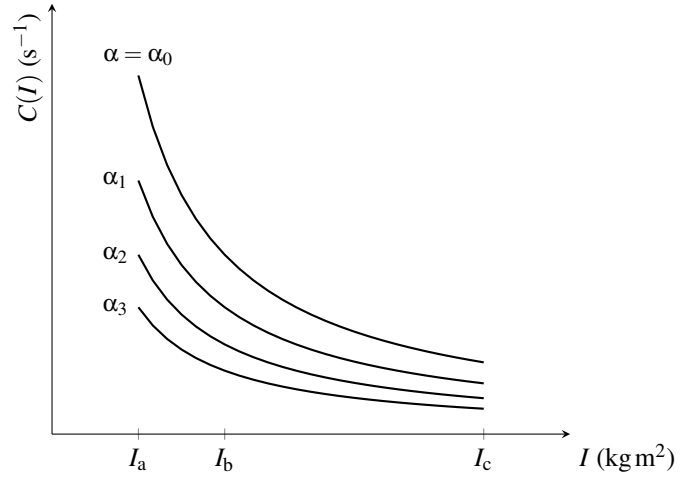

Fig. 3. Illustrative non linear damping model as a function of inertia for different values of α

$$\begin{aligned} C_0(I) &= \frac{1}{C_{01}I} \\[4pt] C_1(I) &= \frac{1}{C_{11}I} \\[4pt] C_2(I) &= \frac{1}{C_{21}I} \\[4pt] C_3(I) &= \frac{1}{C_{31}I} \end{aligned}$$

(40)

2.3.4 Torque Constant Model

It was observed that $\tilde{\beta}$ decreased with increasing α, but the change was not as large, and is modelled by a simple linear approximation:

$$\tilde{\beta}(\alpha, I) = \tilde{\beta}_0(I) + \frac{\tilde{\beta}_1(I) - \tilde{\beta}_0(I)}{\overline{\alpha}_1 - \overline{\alpha}_0}(\alpha - \overline{\alpha}_0) \qquad (41)$$

where $\tilde{\beta}_0$ and $\tilde{\beta}_1$ are the torque constant values at predefined α values $\overline{\alpha}_0$ and $\overline{\alpha}_1$ respectively. In a similar way to the damping in (40), for a given inertia two torque constant values uniquely characterise the torque constant curve. The final model for $\beta(\alpha, I)$ includes models of inertia defined by:

$$\begin{aligned} \tilde{\beta}_0(I) &= \frac{1}{\tilde{\beta}_{01}I} \\[6pt] \tilde{\beta}_1(I) &= \frac{1}{\tilde{\beta}_{11}I} \end{aligned}$$

(42)

2.3.5 Identification of Torque Constant and Damping Model

The parameters $C_{01}, C_{11}, C_{21}, C_{31}, \tilde{\beta}_{01}$ and $\tilde{\beta}_{11}$ cannot be optimised with ordinary least squares since (40) and (42) are non-linear. Therefore, the values of $C_0, \ldots, C_3, \tilde{\beta}_0$ and $\tilde{\beta}_1$ are first optimised for each arm angle to create intermediate "data". The models of (40) and (42) are then inverted and fitted to the intermediate "data" values by ordinary least squares.

The functions $C(\alpha, I)$ and $\tilde{\beta}(\alpha, I)$ in (40) and (42) are fitted by linear least squares to the damping and torque constant data $C_{\text{data}}(\omega)$ and $\beta_{\text{data}}(\omega)$. Note that $C_0 = C_0(I), \ldots, C_3 = C_3(I)$ and $\tilde{\beta}_0 = \tilde{\beta}_0(I), \tilde{\beta}_1 = \tilde{\beta}_1(I)$ are treated as global constants, since I is fixed in this case. For the case of β this process involves fitting a linear line to β_{data}.

2.4 Numerical Simulation & Verification
2.4.1 Non-Linear State Space Model

For verification, the true response of the device is compared against a simulation using the identified parameters. The numerical solution uses similar techniques to the 'quasi-linearisation' technique of Kagiwada [28], where the time variable state space coefficients are recalculated each time step. The actual coefficient values of C and $\tilde{\beta}$ are calculated from the linear model and the estimated α-invariant. The second derivative of the input and the α-invariant values are calculated by iterating through the governing equation of the system until all quantities converge to the larger of either an absolute tolerance or a relative tolerance. To perform the simulation, (37) is converted to a state space form:

$$\dot{\theta} = \Phi$$
$$\dot{\Phi} = -C(\alpha(t))\Phi + \tilde{\beta}(\alpha(t))v(t)$$
$$\alpha(t) = \dot{v}^2 - v\ddot{v} \tag{43}$$
$$v(t) = k_p(r(t) - \theta(t))$$

Equation (43) cannot be solved directly for θ and Φ since α is dependent on $\ddot{v}$, which is dependent on $\ddot{\theta}$. Let C_{linear} and $\tilde{\beta}_{\text{linear}}$ be the global linear model parameters for the given inertia I from (24) and (25). Define the ith approximation to α at $t = t_0$ by:

$$\alpha_{\text{approx}}^{(i)}(t_0) = \dot{v}^2(t_0) - v(t_0)\ddot{v}_{\text{approx}}^{(i-1)}(t_0)$$
$$C_{\text{approx}}^{(i)}(t_0) = C(\alpha_{\text{approx}}^{(i)}(t_0))$$
$$\tilde{\beta}_{\text{approx}}^{(i)}(t_0) = \tilde{\beta}(\alpha_{\text{approx}}^{(i)}(t_0))$$
$$\dot{\Phi}_{\text{approx}}^{(i)}(t_0) = -C_{\text{approx}}^{(i)}(t_0)\Phi(t_0) + \tilde{\beta}_{\text{approx}}^{(i)}(t_0)v(t_0)$$
$$\ddot{v}_{\text{approx}}^{(i)}(t_0) = k_p \cdot (\ddot{r}(t_0) - \dot{\Phi}_{\text{approx}}^{(i)}(t_0)), \quad i = 1, 2, \ldots, N$$

$$\tag{44}$$

$$\ddot{v}_{\text{approx}}^{(0)}(t_0) = -C_{\text{linear}}\Phi + \tilde{\beta}_{\text{linear}}v(t_0) \tag{45}$$

For the given initial starting approximation (45), $\alpha_{\text{approx}}^{(i)}$ is updated at each iteration $i = 1, 2, \ldots, N$ until the following stopping condition is met:

$$|\alpha_{\text{approx}}^{(i)} - \alpha_{\text{approx}}^{(i-1)}| < \max\left(10^{-6}, 10^{-3}|\alpha_{\text{approx}}^{(i)}|\right) \tag{46}$$

Equation (46) stops the iterative algorithm when α_{approx} has converged to within 10^{-6} or 0.1%, whichever is larger. The absolute stopping condition is added to ensure the stopping condition calculation remains numerically stable when $|\alpha_{\text{approx}}| \to 0$. The tolerances were chosen empirically and in all cases gave rapid convergence with only a few iterations

required.

2.4.2 Sinusoidal Steady State Analysis

Sinusoidal steady analysis for the Phantom Omni was performed using the frequencies $[1.5, 2, 2.5, 3, 3.5, 4, 5, 6, 7]$ Hz, in a variety of arm positions as shown in Table 1.

Table 1. Phantom Arm Joint Angles for Frequency Response

Experiment 1 - Frequency Response	
γ_1 **Angle**	γ_2 **Angles**
25°	70°, 90°, 115°
45°	70°, 90°, 115°
65°	70°, 90°, 115°

2.4.3 Step Response

The dynamic parameters from the sinusoidal steady state data is validated against a step response. In particular, these step responses include a number of unique arm positions that were not used in the tuning of parameters from the sinusoidal responses of Table 1. The step response data is obtained by driving the base with a square wave with a frequency of 0.25 Hz and amplitude of 0.07 rad for a set of fixed γ_1 and γ_2 joint angles as shown in Table 2. Although a square wave is not the same as a step, in practice the square wave response can be considered a step response as the frequency is low enough for the Phantom Omni to settle to its final position during each half cycle. The underlying differential equation is defined:

$$\ddot{\theta} + C\dot{\theta} = \tilde{\beta}v(t)$$
$$v(t) = k_p A_r \cdot (2H(t) - 1) \tag{47}$$

where $H(t)$ is the Heaviside step function, with $\theta(0^-) = -0.07$ and $\theta'(0^-) = 0$.

Table 2. Phantom Arm Joint Angles for Step Response

Experiment 2 - Step Response	
γ_1 **Angle**	γ_2 **Angles**
25°	60°, 70°, 90°, 110°, 115°
35°	60°, 70°, 90°, 110°, 115°
45°	60°, 70°, 90°, 110°, 115°
55°	60°, 70°, 90°, 110°, 115°
65°	60°, 70°, 90°, 110°, 115°

3 Phantom Omni Results & Discussion

Two sets of experiments were performed on the Phantom Omni to test the α-invariant model. The experiments were sinusoidal steady state responses for identifying model parameters, and step responses for testing the accuracy of the identified parameters. The frequency response experiments were performed the joint angle positions in Table 1. The accuracy of the sine wave derived model parameters was tested by modelling the response to a 0.25 Hz square wave in the joint angle positions given in Table 2. The square wave fre-

quency was selected low enough so that the square wave response could be interpreted as a series of step responses.

3.1 Inertia and Damping Model

Table 3 shows the raw data used for fitting the inertia model coefficients. The data used is the 'True Angle' and 'Fitted' columns respectively. The $\overline{C}_0$ ratio is calculated by a simple linear regression between the fitted C_{linear} and $\tilde{\beta}_{\text{linear}}$. The true angles in Table 3 are different than the set point angles, due to the face the arm joint angles were controlled with proportional controllers with a constant gravity load. However, as long as the arm joint angles are constant their absolute accuracy is less important, as the measured arm joint angles were used for determining the inertia model coefficients.

Table 3. Frequency Response Calculated from Global Linear Model of C_{linear} and $\tilde{\beta}_{\text{linear}}$

Set Angle		True Angle		Fitted	
γ_1	γ_2	γ_1	γ_2	C_{linear}	$\tilde{\beta}_{\text{linear}}$
25	70	21.54	69.54	5.890	231.53
25	90	20.55	88.54	4.728	177.35
25	115	19.31	112.44	4.288	149.43
45	70	40.68	68.52	5.998	226.42
45	90	39.83	87.63	4.901	176.06
45	115	39.16	111.98	4.612	154.47
65	70	60.68	67.62	7.185	275.32
65	90	60.08	87.00	6.275	222.82
65	115	59.56	111.45	5.915	207.83
		$\overline{C}_0$ Ratio		36.727	

Table 4 shows the matched coefficients of the modified inertia model, offset angle and damping ratio from matching the fitted $\tilde{\beta}_{\text{linear}}$ and C_{linear} in Table 3 using the non-linear regression (28) and (29).

Table 4. Experimentally Determined Inertia Model Parameters for Equation (6) and Damping

Quantity	$n = 0$
I_{base}	$1.063 \cdot 10^{-3}$
I_1	$1.401 \cdot 10^{-3}$
I_2	$2.889 \cdot 10^{-3}$
I_3	$9.392 \cdot 10^{-4}$
γ_{offs}	$9.931°$
$\overline{C}_0$	36.693

Table 5 is a summary of the input and output data from the inertia modelling. It is pleasing to see the fitted and modified inertias all match closely, as well as the damping ratio. This shows the simplified inertia and damping model (6)-(8) is capable of accurately capturing the linearised dynamics of the Phantom Omni.

Table 5. Frequency Response Calculated from Global Linear Model of C_{linear} and $\tilde{\beta}_{\text{linear}}$

Set Angle		True Angle		Fitted		Modelled	
γ_1	γ_2	γ_1	γ_2	C_{linear}	$\tilde{\beta}_{\text{linear}}$	C_{linear}	$\tilde{\beta}_{\text{linear}}$
25	70	21.54	69.54	5.890	231.53	6.061	222.41
25	90	20.55	88.54	4.728	177.35	4.876	178.90
25	115	19.31	112.44	4.288	149.43	3.955	145.12
45	70	40.68	68.52	5.998	226.42	6.122	224.65
45	90	39.83	87.63	4.901	176.06	5.048	185.23
45	115	39.16	111.98	4.612	154.47	4.329	158.86
65	70	60.68	67.62	7.185	275.32	7.229	265.26
65	90	60.08	87.00	6.275	222.82	6.242	229.04
65	115	59.56	111.45	5.915	207.83	5.821	213.59
		$\overline{C}_0$ Ratio		36.727		36.693	

Fig. 4 and Fig. 5 show the inertia model fits against the identified data, and show the inertia model developed in Section 2.1.2 is a good representation of the inertial properties of the Phantom Omni.
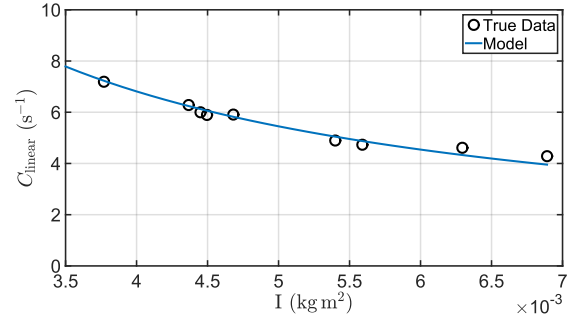

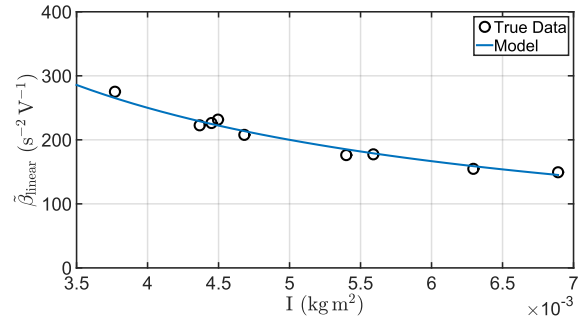Fig. 4. C as a function of inertia

Fig. 5. $\tilde{\beta}_{\text{linear}}$ as a function of inertia

3.2 Non-Linear Resonance and Damping

Fig. 6 and Fig. 7 show the model fits of (40) and (42) to the intermediate damping and torque constant data. The numerical values are given in Table 6 and Table 7. Fig. 6 and Fig. 7 show the model fits for C and $\tilde{\beta}$ respectively. The data is validated by the fact the linear C and β curves are within the range of values of the α-invariant that was measured.
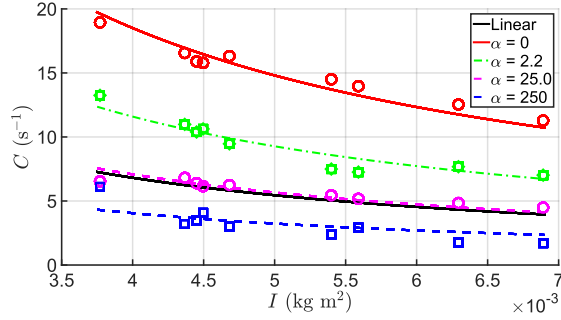
Fig. 6. Non-linear C model as a function of inertia I with Global Linear Model for comparison
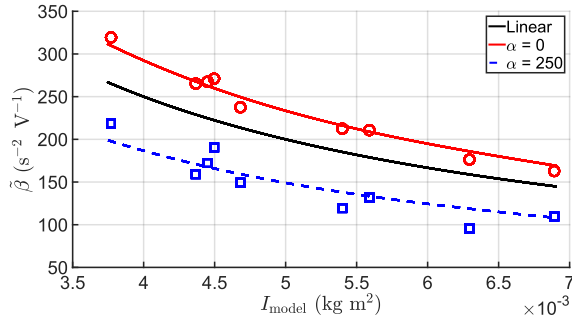

Fig. 7. Non-linear $\tilde{\beta}$ model as a function of inertia I with Global Linear Model for comparison

Table 6. Non-linear $\tilde{\beta}$ model parameters

Quantity	α value	Value
$\tilde{\beta}_{01}$	0	1.3405
$\tilde{\beta}_{11}$	250	0.8558

Table 7. Non-linear C model parameters

Quantity	Value	α value	Ratio to Identified $\overline{C}_0$
C_{01}	61.733	0	1.68238
C_{11}	35.316	2.2	0.96245
C_{21}	21.570	25	0.58783
C_{31}	13.509	250	0.36816

Table 8 shows the simulation error results from the linear model and the α-invariant model for the sine wave frequency sweep. The magnitude error is the absolute difference in response magnitude. The data in Table 8 shows a clear improvement in both magnitude error and phase error with the α-invariant model.

Table 8. Comparison of 90th Percentile Absolute Errors on Magnitude and Phase Angle for Linear and Non-Linear Models

Setpoint		90th Percentile Linear		90th Percentile Non-Linear	
γ_1	γ_2	Magnitude	Phase (°)	Magnitude	Phase (°)
25	70	0.6410	12.1902	0.4146	6.3605
25	90	0.4776	19.4772	0.2756	2.7394
25	115	0.4737	10.6066	0.1935	3.4813
45	70	0.5002	13.2881	0.2202	2.1805
45	90	0.3675	25.3134	0.5202	7.3346
45	115	0.5762	15.0195	0.5173	4.3214
65	70	0.3939	14.0549	0.3714	13.9204
65	90	0.4312	16.2316	0.2028	2.7323
65	115	0.3403	14.3577	0.2968	5.9665
Average		0.4668	15.6155	0.3347	5.4485

3.3 Sinusoidal Frequency Response - Detailed

The parameters $C_{\text{data}}(\omega)$ and $\beta_{\text{data}}(\omega)$ are determined from (19) and (20) and represent the damping and torque constants derived from the data, and are referred to as "measured data". The mean α-invariant is computed for each frequency using (36) and is referred to as $\alpha_{\text{data}}(\omega)$. Fig. 8 shows the α-invariant. The α-invariant increases up to resonance, then decreases as the frequency goes up, due to the decreasing amplitude.
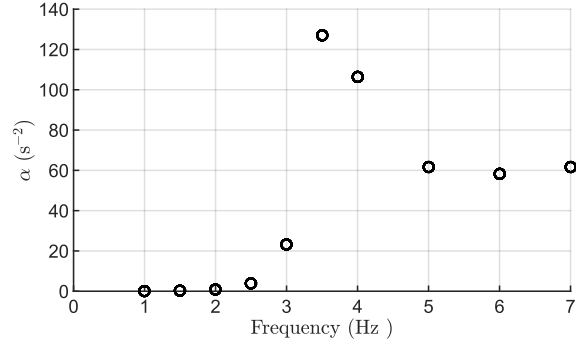

Fig. 8. α-invariant as a function of frequency

The global linear model parameters C_{linear} and β_{linear} are computed by solving (22), and are shown in Table 9.

Table 9. Linear Model Parameters for $\gamma_1 = 65°, \gamma_2 = 90°$

Quantity	Fitted	Modelled
C_{linear}	6.275	6.242
β_{linear}	445.6	458.0
$\tilde{\beta}_{\text{linear}}$	222.8	229.0

The resulting values of $C_0, \ldots, C_3, \tilde{\beta}_0, \tilde{\beta}_1$ and the predefined α values are given in Table 10.

Table 10. Model parameters for $\gamma_1 = 65°, \gamma_2 = 90°$

Quantity	Value
I	0.004366
C_0	16.955
C_1	10.619
C_2	6.486
C_3	3.710
$\tilde{\beta}_0$	267.6
$\tilde{\beta}_1$	170.9

Fig. 9 and 10 show the resulting damping and torque

constant models versus the measured data as well as the data for the global linear approximation. The results of non-linear damping model of (37) were obtained by simulating using (43) - (45).
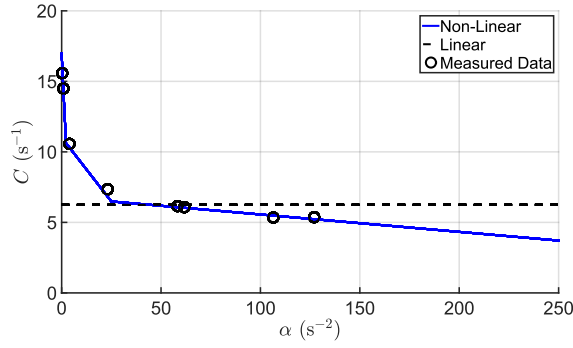

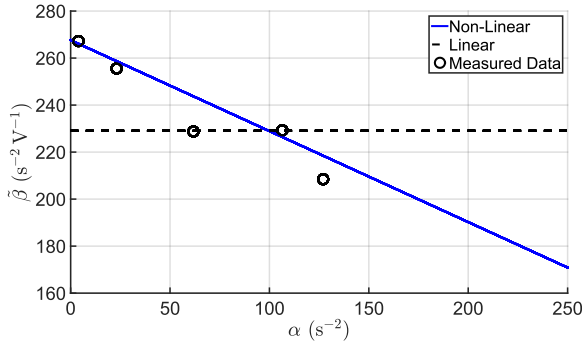Fig. 9. C as a function of α-invariant at $\gamma_1 = 65°$, $\gamma_2 = 90°$

Fig. 10. $\tilde{\beta}$ as a function of α-invariant at $\gamma_1 = 65°$, $\gamma_2 = 90°$

The equivalent non-linear model magnitude and phase values for each frequency are computed by fitting sine waves to the resulting output waveforms, and comparing to the input. Fig. 11 and Fig. 12 show the magnitude and phase responses of the non-linear model of (37) and global linear model of (21) plotted against the measured data.
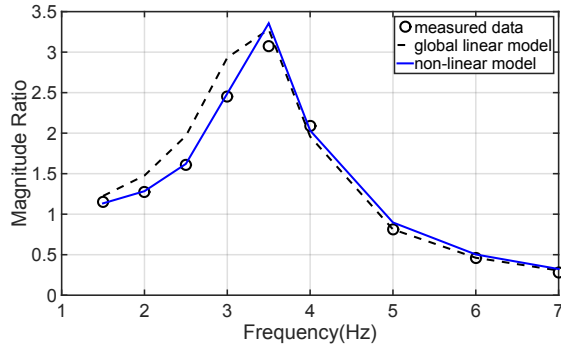

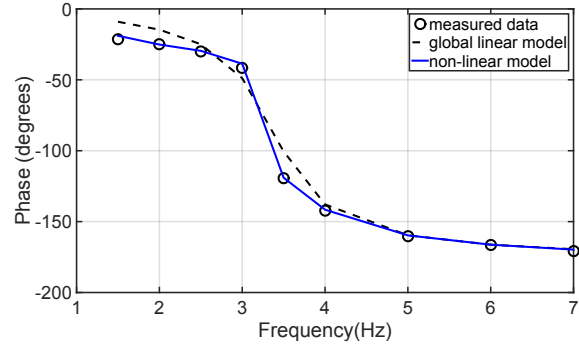Fig. 11. Fundamental Frequency magnitude response for $\gamma_1 = 65°$, $\gamma_2 = 90°$

Fig. 12. Fundamental Frequency phase response for $\gamma_1 = 65°$, $\gamma_2 = 90°$

It is of note that the frequencies of 3-4.5 Hz are used for the linear system identification, based on the intercepts of the nonlinear and linear curves in Fig. 9 and Fig. 10. The linear resonant frequency of 3.4 Hz is within this range, so the linear and α-invariant models are valid with each other, in the sense that the linear coefficients are within domain of the α-invariant coefficients. Fig. 13 shows the response at 2.5 Hz, with the linear and non-linear approximations. All of the bode, phase and time plots demonstrate a significant improvement in modelling accuracy with the α-invariant formulation over the linear formulation.
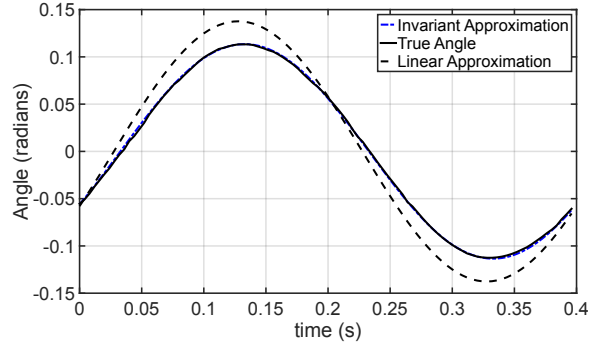

Fig. 13. Time domain response comparison for $\gamma_1 = 65°$, $\gamma_2 = 90°$ at $f = 2.5$ Hz

3.4 Step Response

Fig. 14 shows the first second of the response of the Phantom Omni to the negative-to-positive transition of a 0.25 Hz square wave, which is described by (47).

The non-linear model captures transient behaviour more accurately than the linear model, in particular the non-linear model is better at capturing the increasing damping as the overshoot settles. Table 11 shows the median and 90th percentile for absolute angle error figures for all the step response experiments of Table 2. The increasing errors with increasing γ_2 are due to the larger effect inaccuracies in the inertia model approximation of Link 2 and the Stylus. While putting the centre of mass of the combined Link 2 and Stylus on the axis of Link 2 does contribute the errors seen in Table 11 the errors are reduced from when the centre of mass is put in the 'true' location.
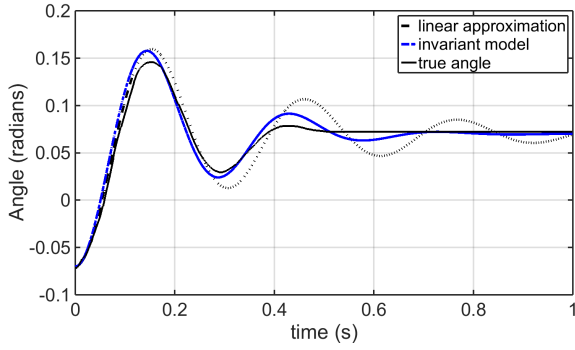
Fig. 14. Comparison of time domain responses to a step input for $\gamma_1 = 65°$, $\gamma_2 = 90°$

Table 11. Absolute Error Percentile Results for Step Response

		Absolute Angle Errors (radians)			
		Lin Abs Error		Invariant Abs Error	
γ_1	γ_2	Median	90th Pctile	Median	90th Pctile
25	60	0.0083	0.0207	0.0036	0.0123
25	70	0.0098	0.0230	0.0045	0.0138
25	90	0.0120	0.0276	0.0067	0.0157
25	110	0.0138	0.0314	0.0082	0.0160
25	115	0.0145	0.0320	0.0087	0.0167
35	60	0.0075	0.0217	0.0021	0.0068
35	70	0.0099	0.0230	0.0029	0.0078
35	90	0.0140	0.0270	0.0036	0.0088
35	110	0.0167	0.0293	0.0041	0.0100
35	115	0.0175	0.0298	0.0043	0.0096
45	60	0.0087	0.0206	0.0030	0.0109
45	70	0.0097	0.0230	0.0036	0.0119
45	90	0.0118	0.0270	0.0058	0.0138
45	110	0.0133	0.0298	0.0073	0.0150
45	115	0.0137	0.0303	0.0076	0.0156
55	60	0.0070	0.0265	0.0020	0.0092
55	70	0.0088	0.0259	0.0025	0.0093
55	90	0.0120	0.0256	0.0037	0.0090
55	110	0.0137	0.0270	0.0037	0.0091
55	115	0.0139	0.0271	0.0036	0.0093
65	60	0.0066	0.0192	0.0023	0.0089
65	70	0.0078	0.0209	0.0024	0.0111
65	90	0.0097	0.0231	0.0034	0.0118
65	110	0.0108	0.0235	0.0037	0.0126
65	115	0.0112	0.0238	0.0041	0.0129
Medians		0.0113	0.0256	0.0043	0.0115

The median of each non-linear response is 2.6 times more accurate than the linear predicted response. Out of the 25 experiments, there are 16 joint arm angle combinations that had no sine wave generated data. These results show the α-invariant modelling approach is applicable to capturing yaw dynamics across the range of arm angle combinations of the Phantom Omni.

4   Conclusions

This paper introduces the α-invariant based energy formulation for characterising a non-linear actuator gain and damping, and tests the model on the response of the Phantom Omni. The α-invariant is an invariant of any pure sine wave input and is proportional to the area of the ellipse in phase space or equivalently the energy dissipated during one cycle.

To make the model truly 'global', an inertia model has been developed to relate different dynamic parameter values at different arm angles. The results obtained show the mean energy as described by the α-invariant of the input to the Phantom Omni's base actuator is useful for characterising the behaviour of the resonant frequency and damping. The dependence of the damping on friction manifested itself as increasing damping with decreasing α-invariant. The work presented in this paper is a good starting point for proving the α-invariant concept, as it is used in a scenario that experiences the compounded effects of non-linearities from the arm segments and other driven parts of the arm attached to the base.

The α-invariant method shows great promise, due to its ability to synthesise an accurate non-linear model from a small set of experiments, and apply these in real time using a simple ODE or state space model. The inertia model uses a simple but rigorous formulation, which is scalable to larger hydraulic machines such as excavators. Apart from scaling the algorithm, the main challenge of transferring the knowledge from the Phantom Omni to a hydraulic machine is taking into account the different actuation systems used in an excavator. Work on developing a minimal model for a laboratory based electro-hydraulic system is in progress and is showing promising results for accuracy.

References

[1] Tahmasebi, A. M., Taati, B., Mobasser, F., and Hashtrudi-Zaad, K., 2005. "Dynamic Parameter Identification and Analysis of a PHANToM TM Haptic Device". In Proceedings of the 2005 IEEE Conference on Control Applications, pp. 1251–1256.

[2] Taati, B., Tahmasebi, A. M., and Hashtrudi-Zaad, K., 2008. "Experimental Identification and Analysis of the Dynamics of a PHANToM Premium 1.5A Haptic Device". *Presence,* **17**(4), pp. 327–343.

[3] Calanca, A., Capisani, L. M., Ferrara, A., and Magnani, L., 2011. "MIMO closed loop identification of an industrial robot". *IEEE Transactions on Control Systems Technology,* **19**(5), pp. 1214–1224.

[4] Marton, L., and Lantos, B., 2011. "Control of robotic systems with unknown friction and payload". *IEEE Transactions on Control Systems Technology,* **19**(6), pp. 1534–1539.

[5] Gautier, M., Janot, A., and Vandanjon, P. O., 2013. "A new closed-loop output error method for parameter identification of robot dynamics". *IEEE Transactions on Control Systems Technology,* **21**(2), pp. 428–444.

[6] Chen, Y.-Y., Huang, P.-Y., and Yen, J.-Y., 2002.

"Frequency-Domain Identification Algorithms for Servo Systems With Friction". *IEEE Transactions on Control Systems Technology,* **10**(5), pp. 654–665.

[7] Hann, C. E., Chase, J. G., Ypma, M. F., Elfring, J., Nor, N. M., Lawrence, P., and Shaw, G. M., 2008. "The Impact of Parameter Identification Methods on Drug Therapy Control in an Intensive Care Unit". *The Open Medical Informatics Journal,* **2**, pp. 92–104.

[8] Moorhead, K. T., Paeme, S., Chase, J. G., Kolh, P., Pierard, L., Hann, C. E., Dauby, P. C., and Desaive, T., 2013. "A simplified model for mitral valve dynamics.". *Computer methods and programs in biomedicine,* **109**(2), Feb., pp. 190–6.

[9] Hann, C. E., Snowdon, M., Rao, A., Winn, O., Wongvanich, N., and Chen, X., 2011. "Minimal modelling approach to describe turbulent rocket roll dynamics in a vertical wind tunnel". *Proceedings of the Institution of Mechanical Engineers, Part G: Journal of Aerospace Engineering,* **226**(9), Dec., pp. 1042–1060.

[10] Wongvanich, N., 2013. "Non linear electromechanical cart characterization using minimal modeling approach". In 2013 Control Conference (ECC), pp. 2927–2932.

[11] Gunn, C., and Zhu, D., 2010. "Haptic Tele-operation of Industrial Equipment". *Proceedings - APCHI-ERGOFUTURE 2010*, p. 6.

[12] Okamura, A. M., 2004. "Methods for haptic feedback in teleoperated robot-assisted surgery.". *The Industrial Robot,* **31**(6), Dec., pp. 499–508.

[13] Ghanbari, A., Abdi, H., Horan, B., Nahavandi, S., Chen, X., and Wang, W., 2010. "Haptic Guidance for Microrobotic Intracellular Injection". In Proceedings of the 2010 3rd IEEE RAS & EMBS, pp. 162–167.

[14] Kim, S.-G., and Sitti, M., 2006. "Task-based and stable telenanomanipulation in a nanoscale virtual environment". *Automation Science and Engineering, IEEE Transactions on,* **3**(3), pp. 240–247.

[15] Kim, S.-m., 2014. "Lumped Element Modeling of a Flexible Manipulator System". *IEEE/ASME Transactions on Mechatronics*(99), pp. 1–8.

[16] Sansanayuth, T., Nilkhamhang, I., and Tungpimolrat, K., 2012. "Teleoperation with Inverse Dynamics Control for PHANToM Omni Haptic Device". In SICE Annual Conference 2012, SICE, pp. 2121–2126.

[17] Mohammadi, A., 2011. "Disturbance Observer Design for Robotic and Telerobotic Systems". PhD thesis, University of Alberta, Edmonton, Alberta.

[18] Na, B., Choi, H., and Kong, K., 2014. "Design of a Direct-Driven Linear Actuator". *IEEE/ASME Transactions on Mechatronics*(99), pp. 1–10.

[19] Armstrong-Hélouvry, B., Dupont, P., and De Wit, C. C., 1994. "A survey of models, analysis tools and compensation methods for the control of machines with friction". *Automatica,* **30**(7), July, pp. 1083–1138.

[20] Rahmat, M., Sunar, N. H., Salim, S. N. S., Abidin, M. S. Z., Fauzi, A. A. M., and Ismail, Z. H., 2011. "Review on Modeling and Controller Design". *International Journal on Smart Sensing and Intelligent Systems,* **4**(4), pp. 630–661.

[21] Berger, E., 2002. "Friction modeling for dynamic system simulation". *Applied Mechanics Reviews,* **55**(6), pp. 535–577.

[22] Van Geffen, V., 2009. A study of friction models and friction compensation. Tech. Rep. DCT2009.118, Technische Universiteit Eindhoven, Eindhoven.

[23] Osman, K., Fauzdi, A., Rahmat, M. F., Mustafa, N., Azman, M. A., and Suzumori, K., 2012. "System Identification Model for an Intelligent Pneumatic Actuator (IPA) System". In IEEE/RSJ International Conference on Intelligent Robots and Systems (IROS), pp. 628–633.

[24] Boulet, B., Daneshmend, L., Hayward, V., and Nemri, C., 2005. "System Identification and Modelling of a High Performance Hydraulic Actuator". In *Lecture Notes in Control and Information Sciences*, G. Chatila, R.; Hirzinger, ed. Springer Verlag, Montreal, pp. 503–520.

[25] Naerum, E., Cornell, J., and Elle, O. J., 2008. "Wavelet Networks for Estimation of Coupled Friction in Robotic Manipulators". In Proceedings of the 2008 IEEE International Conference on Robotics and Automation, pp. 862–867.

[26] Naerum, E., Cornell, J., and Elle, O. J., 2008. "Contact Force Estimation for Backdrivable Robotic Manipulators with Coupled Friction". In Proccedings of the 2008 IEEE/RSJ International Conference on Intelligent Robots and Systems, pp. 22–26.

[27] Lichtsinder, A., and Gutman, P., 2013. "Quasi-linear analytical approach to stick slip friction in the frequency domain". *International Journal of Robust and Nonlinear Control,* **24**(17), pp. 2891–2908.

[28] Bellman, R., Kagiwada, H., and Kalaba, R., 1965. "Quasilinearization, System Identification and Prediction". *International Journal of Engineering Science,* **3**, pp. 327–334.